

# Ultrafast near-field imaging of an operating nanolaser using free electrons

Cléo Santini<sup>1,2</sup>, Thi Huong Ngo<sup>3</sup>, Luiz H. G. Tizei<sup>4</sup>, Aurélie Lloret<sup>2</sup>,  
Tom Fraysse<sup>1</sup>, Sebastien Weber<sup>1</sup>, Adrien Teurtrie<sup>1</sup>, Virginie Brändli<sup>3</sup>,  
Sebastien Chenot<sup>3</sup>, Denis Lefebvre<sup>3</sup>, Stéphane Vézian<sup>3</sup>, Hugo Lourenço-Martins<sup>1</sup>,  
Christelle Brimont<sup>2</sup>, Benjamin Damilano<sup>3</sup>, Thierry Guillet<sup>2</sup>, Sophie Meuret<sup>1\*</sup>

<sup>1\*</sup>CEMES-CNRS, Univ. Paul Sabatier, 29 rue Jeanne Marvig, Toulouse, 31500, France.

<sup>2</sup>L2C, Univ Montpellier, Place Eugène Bataillon, Montpellier, 34095, France.

<sup>3</sup>CRHEA, Univ Côte d'azur, rue Bernard Grégory, Valbonne, 06560, France.

<sup>4</sup>Laboratoire de Physique des Solides, Université Paris-Saclay, CNRS, Orsay, 91405, France.

\*Corresponding author(s). E-mail(s): [sophie.meuret@cemes.fr](mailto:sophie.meuret@cemes.fr);

## Abstract

Integrated opto-electronic devices have the potential to revolutionize information processing, with substantial increase in computing speed, seamless information transfer and reduction of energy consumption. A key missing unit for the successful implementation of compact functional devices are nanometer scale modular and tunable light sources. Monotonically grown semiconducting nanowire lasers (NWLs) fill this gap. However, NWLs operation improvement and optimization require the characterization of their near-field and its dynamics at the nanometer scale, which is hindered due to the light diffraction limit. Here we show how synchronous electron near-field and photon far-field time-resolved spectroscopies surpass this limitation and map a NWLs near-field with nanometer and sub-picoseconds temporal resolution. We quantitatively measured the evolution of the absolute number of stimulated photons  $N_{\mathbf{o}}(t)$  in the NWL cavity, measuring that up to  $4 \times 10^5$  are present simultaneously in the cavity. We mapped the lasing cavity mode's near-field, showing that both whispering gallery and Fabry-Perot modes can participate in the lasing. Our results demonstrate how the near-field of a NWL under operation evolves in the sub-picoseconds and the nanometer scales. We anticipate that a direct observation of the near-field will help to elucidate the influence of materials heterogeneities (defects, chemical changes, contaminants, interface roughness, strain) in NWL operation.

**Keywords:** UTEM, NanoLaser, PINEM, light-matter interaction, out-of-equilibrium spectroscopy

Semiconductors nanowire lasers (NWLs) are one of the most promising new class of nanometer scale light sources, with sub-wavelength applications in bio-sensing and on-chip integrated photonics. Indeed, their monolithic growth insures both a high material quality and an economical viability [1–3]. In addition, their confined cavity mode guarantees a low lasing threshold [4, 5] and ultrafast dynamics [6]. Following the initial experimental demonstration of a ZnO nanowire laser in 2001 [7], NWLs exploiting II-VI, III-V [8, 9], and various other materials [10] have been developed. The abundance of semiconductor gain materials enables a significant tunability for specific applications (wavelength, material compatibility, etc.). One of their most interesting characteristic is that the cavity properties are essentially determined by the geometry of the nanowire, due to the significant refractive index difference between vacuum and semiconductor medium [11]. This means that the lasing wavelength of a NWL is mainly dictated by the cavity length, a design parameter which can be easily tuned [11, 12]. However, despite the dramatic influence of these sub-wavelength parameters, the optical characteristics of nanolasers (e.g. lasing threshold, power density, mono-chromaticity, and lasing dynamics [6]) have up to now only been investigated in the far-field region. There is thus a strong incentive to push the study of NWL in the near-field i.e. accessing the evanescent field with a subwavelength resolution. This was for example achieved on photonic crystal micro-lasers using scanning near-field optical microscopy (SNOM) [13], where an efficient mapping of the luminescence

properties was reported. However, it was also shown that the near-field probe has a strong influence on the measured properties [14], hindering the measurement of intrinsic properties. In this article, we report the first synchronized measurement of far-field and spatially resolved sub-picoseconds temporal dynamics of the optical near-field of NWs during lasing operation. To this aim, we use a combination of micro photo-luminescence spectroscopy ( $\mu$ PL) and photon induced near-field electron microscopy (PINEM) [15] implemented in a custom-built ultrafast transmission electron microscope (UTEM). In the following, we will demonstrate: (1) the quantitative measurement of the absolute number of stimulated photons  $N_0(t)$  inside the NWL cavity as a function of time with sub-picoseconds resolution, and (2) the mapping of the lasing cavity mode's near-field with nanometer resolution.

## 1 PINEM on Nanowire laser

We studied GaN nanowires with 50 nm InGaN inclusions every 150 nm (Fig. 1b). The nanowires are fabricated using a top-down technique (see SI) [3]. The UTEM used in this experiment is a modified Cold-FEG HF3300 Hitachi [16], wherein a 250 fs ultrashort laser pulsed at 2 MHz is directed to both the electron gun to generate a 400 fs pulsed electron beam, and to the sample via a parabolic mirror. The latter enables the efficient excitation of a single NWL with a spot size of approximately 10  $\mu$ m, as well as the collection of its emission spectrum ( $\mu$ PL, see Fig. 1c). Crucially, the electron energy and the  $\mu$ PL spectra are recorded simultaneously, so that the measurements of near- and far-field of the NWs are always correlated. It is particularly important as the stimulated emission of the NWL is marked by the emergence of sharp PL peaks [5] at the cavity modes frequencies (Fig. 1c). The power input vs. intensity output of a typical NWL - in the condition of illumination of the experiment and in a standard micro-photoluminescence ( $\mu$ PL) experiment - are shown in SI (Fig. 6 and Fig. 13).

PINEM is a pump-probe technique where a focused pulsed electron beam probes the z component of the near-field induced by a pulsed laser on a nano-structure (see Fig. 1a). Before this work, in PINEM, the optical modes have always been resonantly excited by the pulsed laser and did not involved light absorption processes. Indeed here, the optical pumping produces electrons and holes relaxing and providing gain, leading to laser emission in a specific electromagnetic mode of the nanowire. When passing through the excited near-field of an object, the electron exchanges quanta of energy with the optical field, resulting in an electron energy spectrum with sidebands spaced by the probed photon energy  $\hbar\omega$  (see Fig. 1d). The amplitude of the  $n^{\text{th}}$  sideband - corresponding to the electrons having exchanged  $n\hbar\omega$  with the field - is noted  $P_n$  with  $n \in \mathbb{Z}$ . Remarkably, all the amplitudes  $P_n$  are uniquely determined by a single quantity - the electron-light coupling constant  $g$  - which can be expressed as [17]:

$$g = \sqrt{N_0} g_0 \quad (1)$$

Here,  $g_0$  denotes the electron-photon scattering amplitude - a mode property independent of the laser excitation - which can be measured by electron energy-loss spectroscopy (EELS) [18]. Therefore, the dynamical properties of the NWL is contained in  $g(t)$  and can be reconstructed by varying the delay  $t$  between the laser pump and the electron probe. The number of photons in the cavity as a function of time  $N_0(t)$  is evaluated from  $g(t)$ .

## 2 Results

### 2.1 Temporal dynamics

We started by focusing the electron beam at a fixed position on the side of the NWL in an aloof geometry and recorded electron energy spectra for each delay  $t$  between the pump laser pulse and the electron probe pulse (Fig. 1b), constructing so-called delay scans. These were recorded for a pumping below ( $P=0.25$  mW) and above ( $P=0.66$  mW) the lasing threshold (Fig. 2). For negative delays  $t < 0$  - corresponding to the probe impinging on the sample before the pump - the electron energy remains unchanged, and only the so-called zero-loss peak (ZLP) is observed, as expected.

Below the lasing threshold (Fig. 2a), the delay scan displays several energy-exchange sidebands around  $t = 0$ . Each sideband has a time-energy correlation due to the electron pulse energy-chirp [19] of 0.89 ps/eV. This chirp is a consequence of the Coulomb repulsion between electrons within the electron pulse [20, 21]. The Coulomb interaction increases the pulse width (from 400 fs to 800 fs), and is taken into account in our models [19]. The energy spacing between each sideband is constant as a function of  $t$  and measured at approximately 3.6 eV. This energy matches the pump laser wavelength, confirming that the electron interacts with the direct scattering of the pump on the surface of the nanowire.

The same *direct scattering* phenomenon is observed when the NWL is pumped above threshold (Fig. 2b). However, a second set of sidebands also appears at  $t > 0.5$  ps. They are separated by approximately 3.3 eV

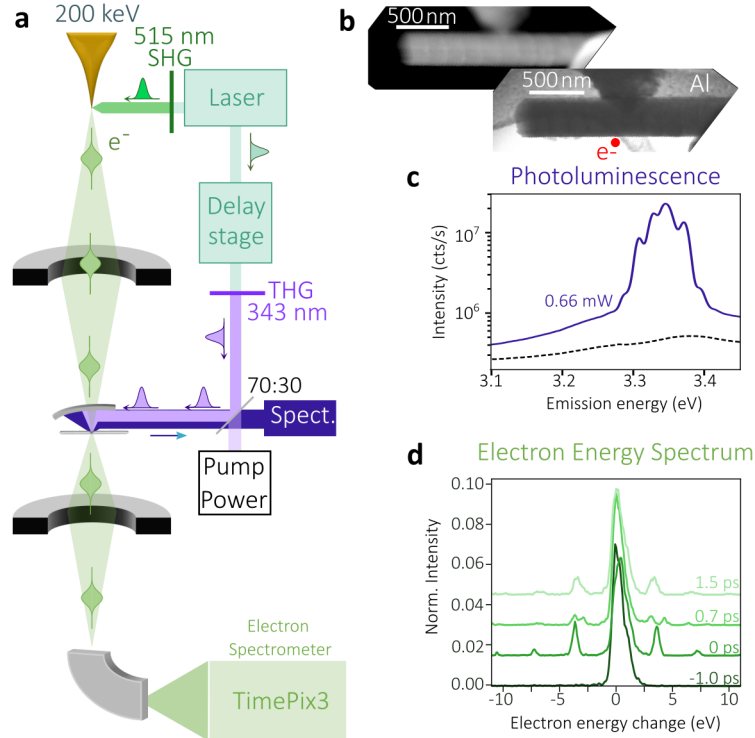


**Fig. 1 Synchronous PINEM and  $\mu$ PL setup.** a) Illustration of the experiment: a 250 fs laser excites a Cold-FEG tungsten tip, resulting in a 2 MHz pulsed electron beam. The third harmonic (THG) of the same fs-laser optically excites the nanolaser above the lasing threshold (here  $P_{th} = 0.66$  mW) via a parabolic mirror placed 200  $\mu$ m above the sample. The photoluminescence is collected using the same parabolic mirror to track the nanolaser’s emission. A motorized delay stage controls the delay between the optical pump and the pulse electron beam (probe). A spectrometer installed with a Timepix3 detector measures the scattered electron energy spectrum. b) Annular Dark Field and Bright Field STEM image of the same NWL under study, the red dot showing the position of the electron beam. c) The NWL photoluminescence spectra, displaying the predicted peaks above the lasing threshold. d) The electron’s energy spectrum after interaction at three distinct delays between the pump and the probe.

which corresponds to the energy of the stimulated emission visible in the PL spectrum (Fig. 1c). This second interaction can thus be identified to be the interaction between the electron beam and the stimulated near-field in the NWL cavity. While several cavity modes are visible on the PL spectra, the spectral resolution ( $\sim 1.0$  eV) of our PINEM setup prevents us from separating them on the electron energy spectra. This is primarily due to the energy dispersion of the electron source used in this experiment.

To confirm our observation, we have simulated the delay scan expected for a lasing NWL with the electron chirp condition of our experiment (Fig. 2c and in SI Fig. 10). Our simulation and experiment display a remarkable agreement when the NWL output laser pulse width is modeled with an exponential decay of characteristic time of  $\tau = 0.76$  ps and an onset time  $t_0 = 0.75$  ps. While the latter is mainly determined by the carriers thermalization, the former is known to be influenced by the cavity geometry and modes [6]. This short lifetime  $\tau$  is in agreement with the expected ultrafast dynamic of nanolasers [22, 23].

## 2.2 Photon population

We attribute the first set of electron energy sidebands ( $t = 0$  ps) to the pump laser light directly scattered at the surface of the nanowire, and the second set of sidebands to the stimulated near-field of the NWLs during lasing. We will now extract the electron-light coupling constant  $g(t)$  from the sidebands amplitude  $P_n$ , starting from the first set of sidebands. Since they correspond to the interaction between an electron pulse (400 fs) which is longer than the light pulse (250 fs), the scattering can be considered incoherent (each electron of the wavepacket experiences a different field). In this case, the sidebands are modeled by a Poisson distribution [24]. The resulting fit of  $g_{scat}(t)$  is shown on Fig. 3a for three different pump powers. This approximation does not apply to the second set of sidebands, where the optical near-field has a long dynamics compared to the electron wavepacket duration. The resulting slight increase in the coherence of the interaction was modeled as in [25] and the resulting  $g_{las}(t)$  is extracted for the same three different pump powers.

The variations of the coupling constant  $g_{las}(t)$  are attributed to the photon population dynamics in the cavity  $N_0(t)$  (equation (1)). To obtain a quantitative estimate of the photon population, we have measured the electron-photon coupling constant  $g_0$  of the same NWL using EELS on a 200 keV monochromated

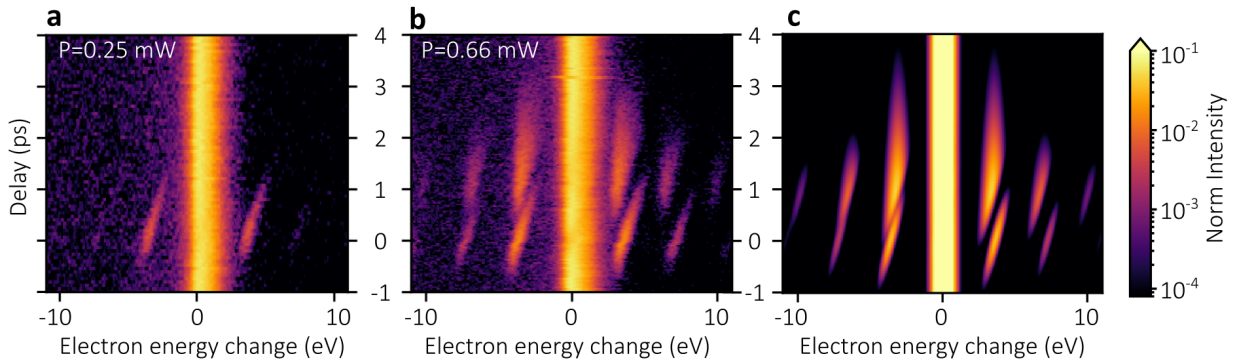


**Fig. 2 PINEM of the stimulated near-field of a NWL.** a), b) Two experimental datasets collected at a fixed position close to the nanolaser for pumping power levels below ( $P=0.25$  mW) and above ( $P=0.66$  mW) the lasing threshold. An electron energy spectrum is recorded every 33 fs delay between the laser pump and the electron probe. The data is normalized using the total intensity for each measurement. The noise visible only in the loss part of the spectrum is consistent with spontaneous electron losses standard in electron energy loss experiment. c) Simulation of b) taking with an onset time of 0.75 ps and a decay time of 0.76 ps for the laser mode and an electron chirp of 0.89 ps/eV.

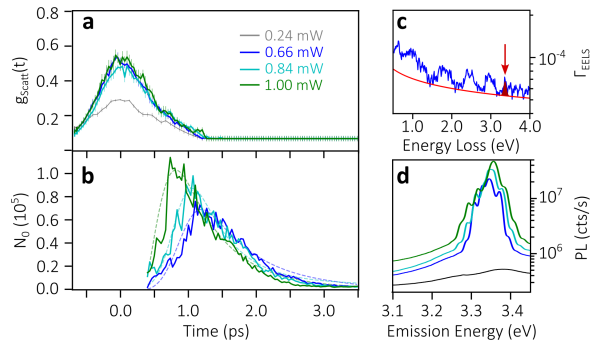


**Fig. 3 Number of photons in the cavity in the lasing regime** a) The electron-near field coupling constant  $g_{scat}$  as a function of pump power at a fixed position. b) Evolution of the number of photons in the cavity,  $N_0(t)$  deduced from  $g_{las}(t)$ , in the lasing regime as a function of the pump power. c) EELS spectrum acquired on the same position as the one where the delay scan of Figure 2 have been acquired (same NWL). d) NWL emission spectrum taken simultaneously than the delay scan for the different pump-powers presented in a-b. The peak corresponding to the lasing mode ( $E = 3.3$  eV) is fitted after removal of the background to extract  $g_0$ : the square root of the red area.

STEM (NION Hermes). The EELS spectrum taken at the same position as the PINEM delay scan is shown on Fig. 3c, a peak at 3.3 eV is clearly visible just below the band gap (marked by a red arrow). More peaks are visible at lower energy corresponding to other cavity modes but not coupled to the bath of spontaneous photons and therefore unavailable for lasing. From this experiment, we have estimated a value of  $g_0 \sim 3.8 \cdot 10^{-3}$  and deduced the photons population dynamic  $N_0(t)$  in the cavity for each pump powers (Fig 3-b).

As expected [26, 27], we observe a clear decrease of the NWL rising time as a function of the pump power (Fig. 3). To further quantify this observation, the extracted  $N_0(t)$  are fitted with an exponential decay convoluted with  $g_{scat}(t)$ , to take the electron chirp into account. The onset time shifts from 0.85 ps at  $P = 0.66$  mW to 0.53 ps at  $P = 1.0$  mW while the NWL pulse width is about 0.6 ps varying from 0.5 ps to 0.7 ps. Moreover, the cavity modes display a slight energy shift with increasing pump power (see the PL spectra in Fig. 3d), changing the ratio between modes, showing that it will be interesting to probe the different modes dynamic with PINEM individually. While our PINEM setup cannot spectrally resolve individual modes, PINEM in state-of-the-art monochromated TEM should reveal this inter-mode dynamics [28]. Due to this lack of spectral resolution we cannot ascertain which of the modes we are actually probing or if all of them are participating to the near-field at this specific electron beam position (see discussion on near-field mapping).

### 2.3 Cavity mode imaging

So far, we have discussed the temporal dynamics of the photon inside the cavity, and will now turn to the spatial mapping of the near field of the lasing mode with sub-wavelength resolution. Indeed, due to their large diameters (between 400 and 500 nm), the NWLs sustain two types of cavity excitation: Fabry-Perot

modes (FPM) and whispering cavity modes (WGM) [29]. The far-field emission pattern is different for both kind of modes and are observed in  $\mu$ PL experiments (see SI).

In order to characterize the near-field profiles of the bare cavity modes (i.e. in absence of external laser pumping), we performed an STEM-EELS hyperspectral imaging experiment on the same monochromated Nion Hermes machine - a technique which had already demonstrated its efficiency in probing such excitations [30, 31]. Fig. 4a shows a typical EELS study of these NWL. The spectrum taken at the side of the NWL exhibits clear peaks that are not visible at the top of the nanowire. We identified the WGM with the clear peaks present in the side while on the top of the NWL only a large number of FPM that almost seems continuous is visible [30]. Fitting the EELS spectrum around 3.3 eV we can separate the contribution of the WGM (amplitude of the peak) and of the Fabry Perot (Amplitude of the continuous background). The different spatial variations of the cavity profile for FPW and WGM are clearly visible and shown on the Fig. 4a for  $E=3.3$  eV.

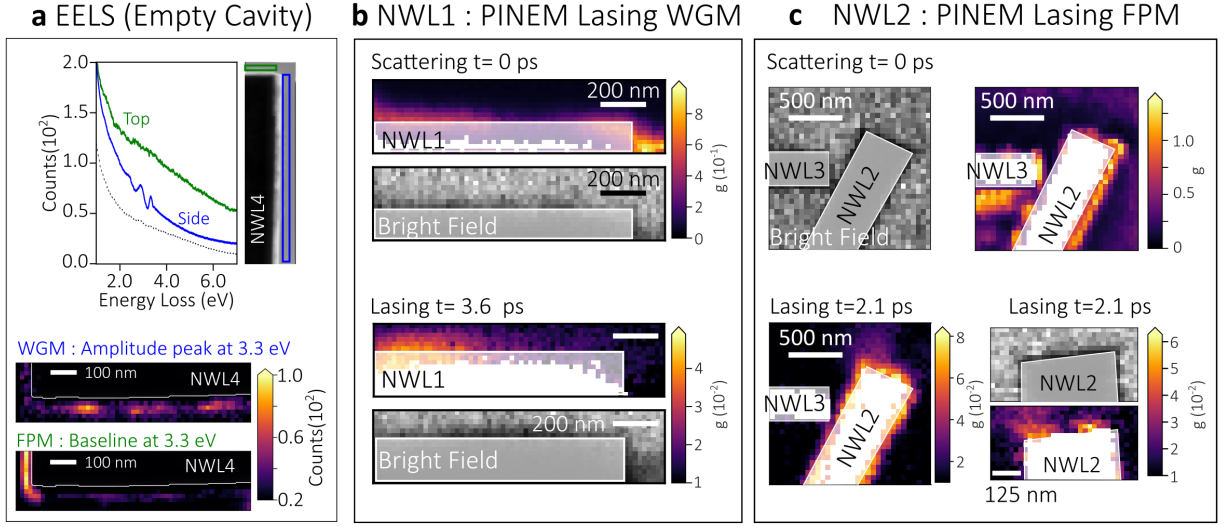


**Fig. 4 Lasing mode spatial profile.** a) Electron energy loss map (without laser pumping) at 200 keV using a monochromated Hermes Nion dedicated STEM on a typical NWL. Spectrum at the top and on the side of the NWL. We see also the fitted map at 3.3 eV b) PINEM on NWL1 : Map of coupling constant ( $g$ ) along the nanolaser at 0 ps delay, with an excitation power of  $P = 0.34$  mW and at  $t = 3.6$  ps at  $P = 0.31$  mW (just above the lasing threshold). The near-field of the lasing mode is here localized on the side of the NWL showing the expected behavior of a whispering gallery mode (WGM). c) PINEM on NWL2 : at  $t = 0$  ps ( $P = 0.94$  mW ) and at  $t = 2.1$  ps ( $P_{th} < P = 0.88$  mW and  $P_{th} < P = 1.2$  mW). The electron coupling constant to the lasing mode ( $g$ ) ( $t = 2.1$  ps) is delocalized along the NWL showing the expected behavior of a Fabry-Perot mode. We can see that the neighboring NWL3 is not lasing. A zoom of the top of NWL2 shows the two expected lobe for a lasing FPM.

We can now image the near-field of the NWL when illuminated by the pump laser above the lasing threshold. To do so, we perform the same PINEM experiment as before albeit here, the pump-probe delay  $t$  is fixed while the impact parameter  $\vec{R}$  of the electron beam is raster-scanned over the nanowire. The resulting  $g(\vec{R})$ -maps for two delays -  $t = 0$  ps (i.e. direct scattering of the pump laser on the nanowire) and  $t = 3.6$  ps (lasing NWL cavity) - are shown on Fig. 4b. The second delay was chosen so because the pump power being slightly above the lasing threshold ( $P = 0.31$  mW), the onset time is of about 2 ps after optical excitation (see SI).

For the first case ( $t = 0$ ), the intensity of the near-field depends on the geometry of the different interfaces, on the aluminum layer below the nanolaser as well as on the angle between the incident light and the sample due to the parabolic mirror [32]. However, for the second case showed ( $t = 3.6$  ps), the induced near-field is drastically different and is clearly localized around two InGaN inclusions, spreading over a distance of 200 nm. By comparison with the EELS experiment (Fig. 4a), we can attribute this near-field profile to a WGM. Nevertheless, other cavity modes can be involved in the lasing, as shown on another NWL (NWL2) Fig. 4c where the near-field display clear features of a FPM - with two lobes located at the end facet. It is also interesting to note here that Fig. 4c shows a neighboring nanolaser (NWL3) that does not lase. PINEM allow us to separate the behavior of two very closely located NWL.

### 3 Conclusion

In conclusion, the spatial and temporal distribution of lasing modes in GaN NWL was mapped with few nanometer and sub-picosecond resolutions using PINEM. Coupled to monochromated EELS, this method

revealed the time-dependent photon population  $N_0(t)$  within the cavity - without *a priori* knowledge on the light collection and focusing power - and the influence of the pump power on the laser rise time. Moreover, we mapped and identified the nature of the modes - FPM or WGM - involved in the lasing regime.

This work represents the first demonstration, of the potential of PINEM to study semiconductors population inversion dynamics, light absorption and field generated. In combination with the analytical capability of conventional TEM, PINEM enables to directly link the material's atomic structure heterogeneity (e.g., defects, impurities, strain), the surrounding environment and the NWL geometry to the optical properties of the NWLs.

It must be stressed that the spatial, temporal, and energy resolutions of the UTEM used in this study are respectively limited to 10 nm, 300 fs, and 1.0 eV, and we therefore expect the new generation of high-resolution instruments [28, 33] to be able to dive even deeper in the physics of nanolasers or into more complex geometries, such as SPASERS [1]. For example, monochromated electron microscopes [28] may be able to resolve challenges related to mode hopping, cavity mode interference, and inter-mode dynamics.

## 4 Methods

**TEM experiments** requires an electron-transparent substrate. The NWLs were therefore deposited on a Holey carbon grid with an evaporated 100 nm Aluminium layer below the Carbon layer (the carbon layer playing the role of spacer between the Al layer and the NWL). This Al layer enables the determination of the pump-probe spatio-temporal overlap and seems to facilitate heat dissipation.

**Electron energy detection scheme in the PINEM experiment** : the electron energy spectrum were recorded using a Gatan PEELS 666 spectrometer with an ASI Cheetah 3 timepix detector (Fig. 1d).

**Acknowledgements.** The author thank Albert Polman and Nika Van Nielen for discussions and preliminary experiments. We also thank Mathieu Kociak for discussions and the all STEM group for their patience when the microscope was blocked at 200 keV. This work received support from the National Agency for Research under the program of future investment TEMPOS-CHROMATEM (ANR-10- EQPX-50). The authors acknowledge financial support from the CNRS-CEA "METSA" French network (FR CNRS 3507) on the platform LPS-STEM. The author acknowledge financial support of the French Agence Nationale de la Recherche (ANR), under the grant agreement ANR-23-CE09-0018 - LUTEM.

## Author Contribution

**C. Santini**, with the assistance of **S. Meuret**, carried out the entire PINEM experiment and data analysis for the study, as well as building a portion of the PINEM setup required for the experiment. **T.H. Ngo** and **B. Damilano** created the samples with assistance from **V. Brändl**, **S. Chenot**, **D. Lefebvre**, and **S. Vézian**. **L. Tizei** carried out the EELS experiment and analyzed the data alongside **S. Meuret**. **T. Fraysse** and **H. Lourenço-Martins** assisted with the PINEM interpretation and data analysis. **S. Weber** and **A. Teurtrie** are in charge of the UTEM experiment and helped build a portion of the setup. **S. Weber** developed the acquisition software PyMoDAQ used in the experiment. **A. Lloret** oversees the optical setup for NWL characterization. **C. Brimont** and **T. Guillet** carried out the optical characterization and supervised the work with **S. Meuret**.

## References

- [1] Ellis, T.C., Eslami, S., Palomba, S.: Nanolasers: More than a decade of progress, developments and challenges **13**(15), 2707–2739 <https://doi.org/10.1515/nanoph-2023-0369> . Accessed 2025-12-03
- [2] Behzadirad, M., Nami, M., Wostbrock, N., Zamani Kouhpanji, M.R., Feezell, D.F., Brueck, S.R.J., Busani, T.: Scalable top-down approach tailored by interferometric lithography to achieve large-area single-mode GaN nanowire laser arrays on sapphire substrate **12**(3), 2373–2380 <https://doi.org/10.1021/acsnano.7b07653> . Accessed 2025-12-03
- [3] Damilano, B., Coulon, P.-M., Vézian, S., Brändli, V., Duboz, J.-Y., Massies, J., Shields, P.A.: Top-down fabrication of GaN nano-laser arrays by displacement talbot lithography and selective area sublimation **12**(4), 045007 <https://doi.org/10.7567/1882-0786/ab0d32> . Accessed 2025-12-02
- [4] Gradečak, S., Qian, F., Li, Y., Park, H.-G., Lieber, C.M.: GaN nanowire lasers with low lasing thresholds **87**(17), 173111 <https://doi.org/10.1063/1.2115087> . Accessed 2025-12-02

- [5] Couteau, C., Larrue, A., Wilhelm, C., Soci, C.: Nanowire lasers **4**(1), 90–107 <https://doi.org/10.1515/nanoph-2015-0005> . Accessed 2025-12-03
- [6] Röder, R., Sidiropoulos, T.P.H., Tessarek, C., Christiansen, S., Oulton, R.F., Ronning, C.: Ultrafast dynamics of lasing semiconductor nanowires **15**(7), 4637–4643 <https://doi.org/10.1021/acs.nanolett.5b01271> . Accessed 2025-12-02
- [7] Huang, M.H., Mao, S., Feick, H., Yan, H., Wu, Y., Kind, H., Weber, E., Russo, R., Yang, P.: Room-temperature ultraviolet nanowire nanolasers **292**(5523), 1897–1899 <https://doi.org/10.1126/science.1060367> . Accessed 2025-12-04
- [8] Johnson, J.C., Choi, H.-J., Knutsen, K.P., Schaller, R.D., Yang, P., Saykally, R.J.: Single gallium nitride nanowire lasers **1**(2), 106–110 <https://doi.org/10.1038/nmat728> . Accessed 2025-12-03
- [9] Saxena, D., Mokkapatil, S., Parkinson, P., Jiang, N., Gao, Q., Tan, H.H., Jagadish, C.: Optically pumped room-temperature GaAs nanowire lasers **7**(12), 963–968 <https://doi.org/10.1038/nphoton.2013.303> . Accessed 2025-12-04
- [10] Yang, Z., Pelton, M., Fedin, I., Talapin, D.V., Waks, E.: A room temperature continuous-wave nanolaser using colloidal quantum wells **8**(1), 143 <https://doi.org/10.1038/s41467-017-00198-z> . Accessed 2025-12-03
- [11] Maslov, A.V., Ning, C.: GaN nanowire lasers. In: Piprek, J. (ed.) Nitride Semiconductor Devices: Principles and Simulation, 1st edn., pp. 467–491. Wiley. <https://doi.org/10.1002/9783527610723.ch21> . <https://onlinelibrary.wiley.com/doi/10.1002/9783527610723.ch21> Accessed 2025-12-03
- [12] Zhuang, X., Ouyang, Y., Wang, X., Pan, A.: Multicolor semiconductor lasers **7**(17), 1900071 <https://doi.org/10.1002/adom.201900071> . Accessed 2025-12-03
- [13] Vo, T.-P., Rahmani, A., Belarouci, A., Seassal, C., Nedeljkovic, D., Callard, S.: Near-field and far-field analysis of an azimuthally polarized slow bloch mode microlaser **18**(26), 26879 <https://doi.org/10.1364/OE.18.026879> . Accessed 2025-12-05
- [14] Le Gac, G., Rahmani, A., Seassal, C., Picard, E., Hadji, E., Callard, S.: Tuning of an active photonic crystal cavity by an hybrid silica/silicon near-field probe **17**(24), 21672 <https://doi.org/10.1364/OE.17.021672> . Accessed 2025-12-05
- [15] Barwick, B., Flannigan, D.J., Zewail, A.H.: Photon-induced near-field electron microscopy **462**(7275), 902–906 <https://doi.org/10.1038/nature08662> . Accessed 2025-12-02
- [16] Houdellier, F., Caruso, G.M., Weber, S., Kociak, M., Arbouet, A.: Development of a high brightness ultrafast transmission electron microscope based on a laser-driven cold field emission source **186**, 128–138 <https://doi.org/10.1016/j.ultramic.2017.12.015> . Accessed 2025-12-04
- [17] Di Giulio, V., Kociak, M., De Abajo, F.J.G.: Probing quantum optical excitations with fast electrons **6**(12), 1524 <https://doi.org/10.1364/OPTICA.6.001524> . Accessed 2025-12-04
- [18] Nelayah, J., Kociak, M., Stéphan, O., García De Abajo, F.J., Tencé, M., Henrard, L., Taverna, D., Pastoriza-Santos, I., Liz-Marzán, L.M., Colliex, C.: Mapping surface plasmons on a single metallic nanoparticle **3**(5), 348–353 <https://doi.org/10.1038/nphys575> . Accessed 2025-12-02
- [19] Park, S.T., Kwon, O.-H., Zewail, A.H.: Chirped imaging pulses in four-dimensional electron microscopy: femtosecond pulsed hole burning **14**(5), 053046 <https://doi.org/10.1088/1367-2630/14/5/053046> . Accessed 2023-10-20
- [20] Haindl, R., Feist, A., Domröse, T., Möller, M., Gaida, J.H., Yalunin, S.V., Ropers, C.: Coulomb-correlated electron number states in a transmission electron microscope beam **19**(10), 1410–1417 <https://doi.org/10.1038/s41567-023-02067-7> . Accessed 2023-10-20
- [21] Feist, A., Bach, N., Rubiano Da Silva, N., Danz, T., Möller, M., Priebe, K.E., Domröse, T., Gatzmann, J.G., Rost, S., Schauss, J., Strauch, S., Bormann, R., Sivis, M., Schäfer, S., Ropers, C.: Ultrafast transmission electron microscopy using a laser-driven field emitter: Femtosecond resolution with a high coherence electron beam **176**, 63–73 <https://doi.org/10.1016/j.ultramic.2016.12.005> . Accessed

- [22] Johnson, J.C., Knutsen, K.P., Yan, H., Law, M., Zhang, Y., Yang, P., Saykally, R.J.: Ultrafast carrier dynamics in single ZnO nanowire and nanoribbon lasers **4**(2), 197–204 <https://doi.org/10.1021/nl034780w> . Accessed 2025-12-02
- [23] Daskalakis, K.S., Väkeväinen, A.I., Martikainen, J.-P., Hakala, T.K., Törmä, P.: Ultrafast pulse generation in an organic nanoparticle-array laser **18**(4), 2658–2665 <https://doi.org/10.1021/acs.nanolett.8b00531> . Accessed 2025-12-02
- [24] Park, S.T., Lin, M., Zewail, A.H.: Photon-induced near-field electron microscopy (PINEM): theoretical and experimental **12**(12), 123028 <https://doi.org/10.1088/1367-2630/12/12/123028> . Accessed 2026-01-23
- [25] Harvey, T.R., Henke, J.-W., Kfir, O., Lourenço-Martins, H., Feist, A., García De Abajo, F.J., Ropers, C.: Probing chirality with inelastic electron-light scattering **20**(6), 4377–4383 <https://doi.org/10.1021/acs.nanolett.0c01130> . Accessed 2026-01-21
- [26] Lorke, M., Suhr, T., Gregersen, N., Mørk, J.: Theory of nanolaser devices: Rate equation analysis versus microscopic theory **87**(20), 205310 <https://doi.org/10.1103/PhysRevB.87.205310> . Accessed 2025-12-02
- [27] Weng, G., Tian, J., Chen, S., Yan, J., Zhang, H., Liu, Y., Zhao, C., Hu, X., Luo, X., Tao, J., Chen, S., Zhu, Z., Chu, J., Akiyama, H.: Electron–hole plasma lasing dynamics in CsPbCl<sub>m</sub>Br<sub>3-m</sub> microplate lasers **8**(3), 787–797 <https://doi.org/10.1021/acsphotonics.0c01512> . Accessed 2025-12-02
- [28] Castioni, F., Auad, Y., Blazit, J.-D., Li, X., Woo, S.Y., Watanabe, K., Taniguchi, T., Ho, C.-H., Stéphan, O., Kociak, M., Tizei, L.H.G.: Nanosecond nanothermometry in an electron microscope **25**(4), 1601–1608 <https://doi.org/10.1021/acs.nanolett.4c05692> . Accessed 2025-12-04
- [29] Coulon, P.-M., Hugues, M., Alloing, B., Beraudo, E., Leroux, M., Zuniga-Perez, J.: GaN microwires as optical microcavities: whispering gallery modes vs fabry-perot modes **20**(17), 18707 <https://doi.org/10.1364/OE.20.018707> . Accessed 2026-03-23
- [30] Du, J., Chen, J.-h., Li, Y., Shi, R., Wu, M., Xiao, Y.-F., Gao, P.: Electron microscopy probing electron-photon interactions in SiC nanowires with ultrawide energy and momentum match **22**(15), 6207–6214 <https://doi.org/10.1021/acs.nanolett.2c01672> . Accessed 2025-12-02
- [31] Auad, Y., Hamon, C., Tencé, M., Lourenço-Martins, H., Mkhitarian, V., Stéphan, O., García De Abajo, F.J., Tizei, L.H.G., Kociak, M.: Unveiling the coupling of single metallic nanoparticles to whispering-gallery microcavities **22**(1), 319–327 <https://doi.org/10.1021/acs.nanolett.1c03826> . Accessed 2026-01-21
- [32] Meuret, S., Lourenço-Martins, H., Weber, S., Houdellier, F., Arbouet, A.: Photon-induced near-field electron microscopy of nanostructured metallic films and membranes **11**(3), 977–984 <https://doi.org/10.1021/acsphotonics.3c01223> . eprint: <https://doi.org/10.1021/acsphotonics.3c01223>
- [33] Schröder, A., Wendeln, A., Weber, J.T., Mukai, M., Kohno, Y., Schäfer, S.: Laser-driven cold field emission source for ultrafast transmission electron microscopy **275**, 114158 <https://doi.org/10.1016/j.ultramic.2025.114158> . Accessed 2025-12-21
- [34] García De Abajo, F.J., Asenjo-Garcia, A., Kociak, M.: Multiphoton absorption and emission by interaction of swift electrons with evanescent light fields **10**(5), 1859–1863 <https://doi.org/10.1021/nl100613s> . Accessed 2025-12-02

## 5 Supplementary Materials

### 5.1 Process for the fabrication of GaN/InGaN nanowires

The structure is first grown using metal-organic vapor-phase epitaxy on a sapphire substrate. It consists of a 3.3  $\mu\text{m}$ -thick GaN layer and a multilayer with 10 periods of In<sub>0.03</sub>Ga<sub>0.97</sub>N (40 nm) / GaN (180 nm). The fabrication process flow is shown in figure 5a-e. Starting with the epitaxial structure (figure 5a), resist

is spin-coated onto the surface, and photolithography is used to create  $1\ \mu\text{m}$ -diameter holes with a  $10\ \mu\text{m}$  pitch (figure 5b). Then,  $150\ \text{nm}$  of Ni is deposited and lifted off to form the hard mask (figure 5c). The III-nitride layers are etched using  $\text{Cl}_2$ -based plasma in an ICP chamber (figure 5d). After etching, the Ni mask is stripped with piranha solution. Subsequently, the nanowires are immersed in a 45 wt.% KOH solution at  $100^\circ\text{C}$  for 50 minutes to smooth their lateral facets and reduce their diameters (figure 5e). This process ultimately results in an array of GaN/InGaN nanowires with a height of  $5.5\ \mu\text{m}$  standing on the sapphire substrate, as depicted in figure 5f.

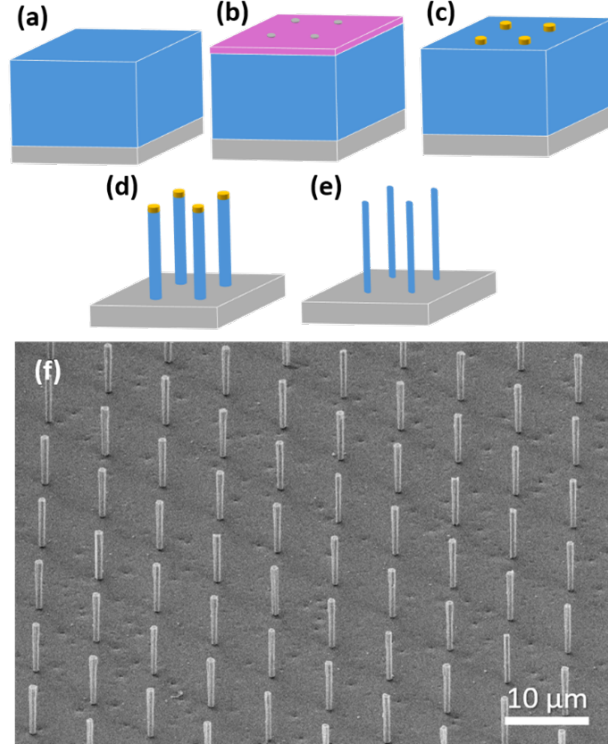


**Fig. 5** (a)-(e) Process flow diagram for nanowire fabrication: (a) growth by metal-organic vapor phase epitaxy on a sapphire substrate; (b) resist spin-coating and photolithography to create  $1\ \mu\text{m}$  diameter holes with a  $10\ \mu\text{m}$  pitch; (c) metallization and lift-off to form a Ni hard mask; (d) dry-etching using  $\text{Cl}_2$ -based ICP; (e) Ni removal with piranha solution followed by KOH wet-etching to smooth the sidewalls and further reduce wire diameters. (f)  $30^\circ$ -tilted SEM images of nanowires standing on the sapphire substrate

## 5.2 Emission S-shape and characterization optic

The nanowire samples are investigated in a standard micro-photoluminescence experiment, where lasing is observed under similar conditions as in the electron microscope: the nanowires are deposited on a membrane and optically pumped at room temperature with the second harmonics of a mode-locked TiSa laser, at  $355\ \text{nm}$  and pulse width of  $150\ \text{fs}$ . The emission is collected with a  $50\times$  microscope objective and imaged onto the entrance slit of the spectrometer, so that the CCD detector provides a spectral and spatial image of the emission along the nanowire axis.

The spectra of the emission extracted at the end and the center of a given nanowire are represented in the figure 6(a,b) as a function of the pump power relative to the nanolaser threshold, and the corresponding images are shown in the panels (c-e). The emission spectrum below threshold is detected under the pump spot and corresponds to the emission of the photo-generated electron-hole pairs in the InGaN sections of the nanowire, at  $3.34\ \text{eV}$ , and its LO-phonon replica at lower energy. At threshold, the lasing mode at  $3.38\ \text{eV}$  is also observed under the pump spot, whereas a second threshold corresponds to the appearance of a pair of lasing modes at  $3.2\ \text{eV}$  that are only detected at the two ends of the nanowire. Therefore the lasing mode at  $3.38\ \text{eV}$  is attributed to a WGM, whereas the ones at  $3.2\ \text{eV}$  corresponds to Fabry-Perot modes.

The lasing configuration depends on the investigated nanowire laser and on the size of the pump spot with respect to the nanowire length: in another nanowire, excited with a longer pump spot, the first lasing threshold correspond to Fabry-Perot modes. These configurations are similar to the two PINEM observations.

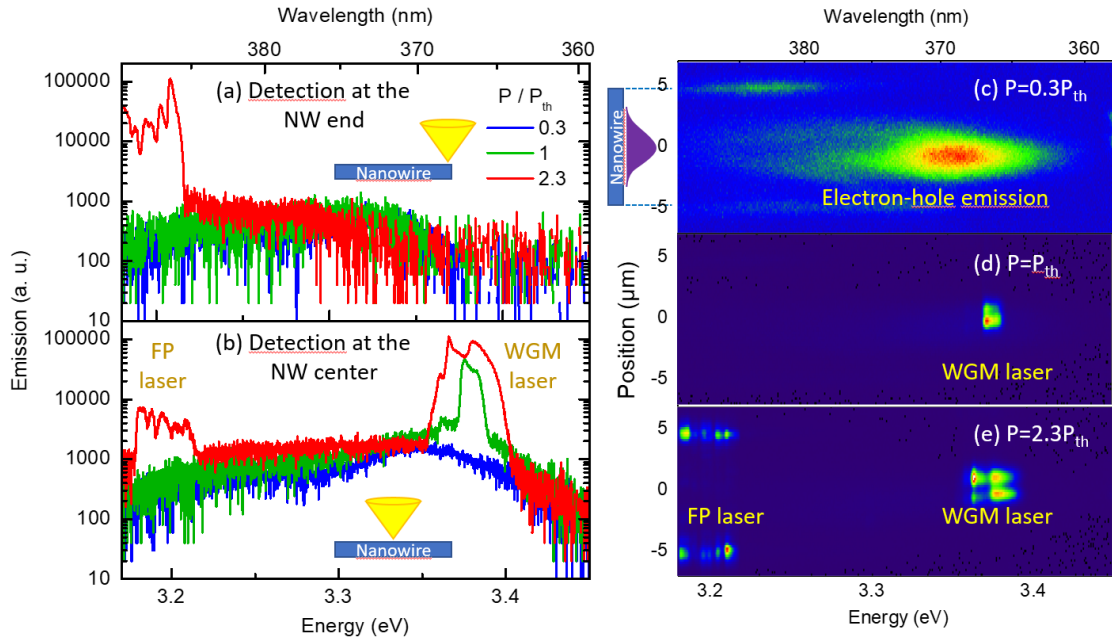


**Fig. 6** Micro-Photoluminescence imaging of the nanowire emission; (a)-(b) Spectra recorded at the end and the middle of the nanowire vs pump power relative to the threshold; (c)-(e) Spatially- and spectrally-resolved images of the nanowire emission, below, at and above threshold

### 5.3 Finding the coupling constant

Everything will be illustrated with the Delay scan corresponding to  $P = 0.66$  mW and presented in Figure 2 of the main text.

#### 5.3.1 Raw Data treatment

The two experimental data sets shown in Figure 2 of the main article are realigned to correct for the fluctuation of the zero-loss position on the spectrometer during dataset acquisition and normalized by the total intensity of the spectrum for each delay to account for photoemission process fluctuations. Figure 7 depicts the transformation of raw data into realigned data.

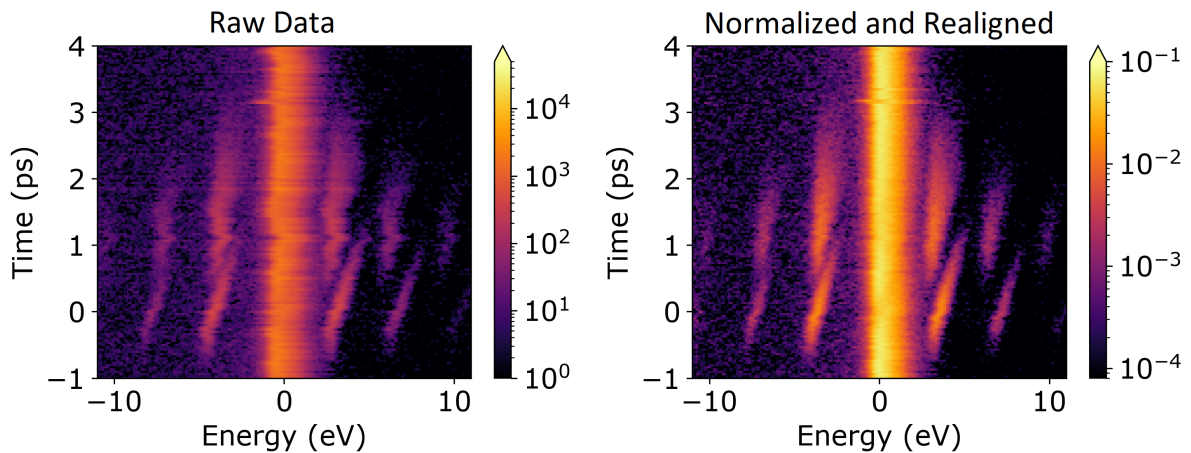


**Fig. 7** Raw Data to Realigned and Normalized Data. Left: Raw Data for a pumping laser power of  $P=0.66$  mW. Right: Processed data as shown on Figure 2 of the main text.

#### 5.3.2 Separating the two different contributions of the Delay scan

Separating the two components allows us to fit the  $g$  from scattering and lasing independently. For this, we use a least squares method with a model with two sets of side bands, with the spacing between the side bands determined by  $E_0$  and  $E_1$ . The amplitudes were free, but the loss and gain of the same  $n^{\text{th}}$  order are

forced to have the same amplitude. We obtain the two sets shown in Figure 8(a). These two sets can be used to retrieve the two coupling constants  $g_{scatt}$  and  $g_{las}$ , as shown in Figure 3 of the main text. One can see that the fit produces some residual side band at long delay; this is an artifact of the fit and accounts for the large error bar at long delay in figure 3 of the main text.

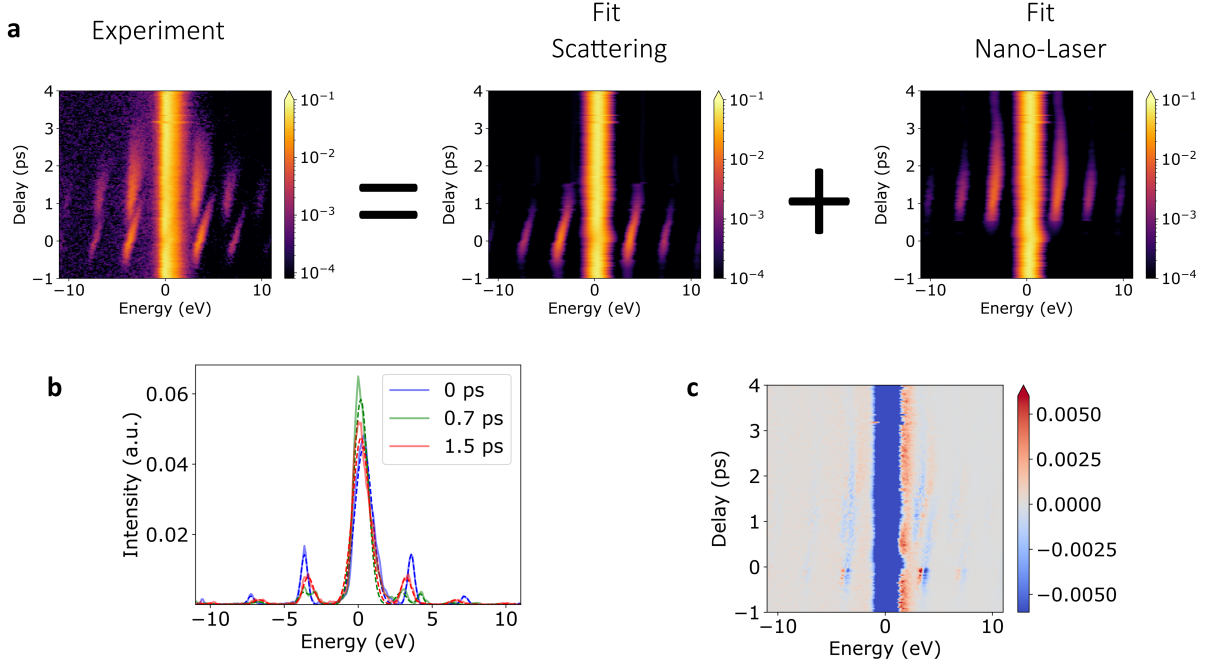


**Fig. 8** a) Two component extracted from Raw Data with fitting procedure  
b) Three extracted spectrum and their respected fits. c) Residual of the fit procedure

### 5.3.3 Fitting the two set of side band with PINEM theoretical model

Once the dataset are fitted with the model of 5.3.2, we fit separately the two set of PINEM interaction found in Figure 8. The scattering interaction is very nicely reproduced using the model of the weak interaction regime developed in [34], where the amplitude  $A_n$  of the order  $n$  is given by :

$$A_n = e^{-2|g|^2} I_n(2|g|^2) \quad (2)$$

Where  $g$  is the coupling constant, and  $I_n$  is the modified Bessel function. Because of the electron chirp, calculating the amplitude of zero loss ( $n = 0$ ) is extremely difficult. As previously stated, we fixed the amplitude of the loss and gain to be identical (see section 8), so we fit the amplitude for  $n > 0$  using the peak on the gain side.

The weak coupling regime cannot reproduce the first-to-second order ratio when interacting with the lasing mode. This could be explained by the longer-lasting field, as well as the difference in lasing field strength between pulses. It is entirely possible that population inversion and stimulated emission do not occur for every pulse. We apply the same model as in [25]. We calculate the value of  $g$  using these two fits (Figure 3 of the main article). Figure 9 depicts the delay scan not shown in the main text, from which the  $g$  for the other pump power was extracted ( $P=0.84$  mW and  $P=1.0$  mW).

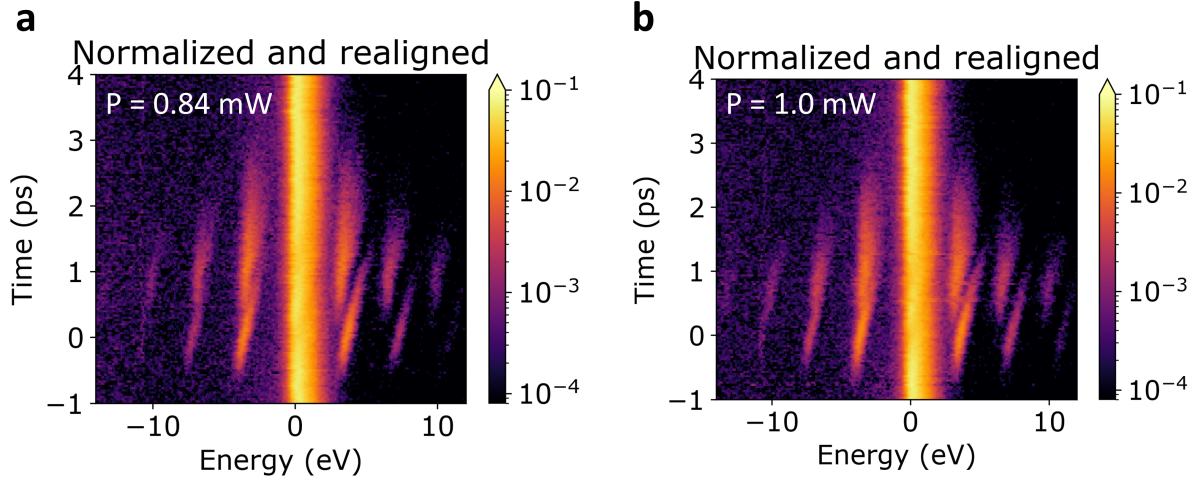


**Fig. 9** Delay scan treated with the procedure explained in section 5.3 for injection power  $P = 0.84$  mW and  $P = 1.0$  mW

#### 5.4 Simulation of the beam Chirp

To simulate the chirp of Figure 2, we convolute the chirp of the electron beam with the PINEM expected using the two models discussed in section 5.3. To simulate the PINEM with no chirp we described the evolution in time of the coupling constant  $g(t)$  (see Figure 10-a) by :

$$g_{Scat}(t) = \frac{A}{\sqrt{2\pi}\sigma_{pump}} e^{-\frac{t^2}{2\sigma_{pump}^2}}$$

$$g_{Las}(t) = \frac{1}{\tau} e^{-\frac{t-t_0}{\tau}} \quad (3)$$

$$g(t) = g_{Scat}(t) + g_{Las}(t)$$

We found the value of the onset time  $t_0 = 0.74$  ps the characteristic time of the NWLs lasing pulse  $\tau = 0.76$  ps by fitting the  $g$  curve of figure 3 of the main article. We then use the two interaction models discussed in section 5.3 , to reproduce the energy spectrum expected at every delay  $t$ . The result is shown on figure 10-b.

The electronic chirp  $P(t, E)$  is defined by [19]:

$$P(t, E) = (1/(2\pi\sigma_t\sigma_E)) * \exp[-(t - s_1E)^2/(2\sigma_t^2)] * \exp[-E^2/(2\sigma_E^2)] \quad (4)$$

where  $\sigma_t$  and  $\sigma_E$  are deduced respectively from the laser pulse width 282 fs and the energy spread of the source 700 meV [16]. We extracted, from the slot of the first side band of the scattering interaction on the experimental data, a chirp of  $s_1 = 0.89$  ps/eV).

We then convolute the two resulting 2D map (depicted in Figure 10) to obtain the simulated delay scan of Figure 2 and reproduced Figure 10.

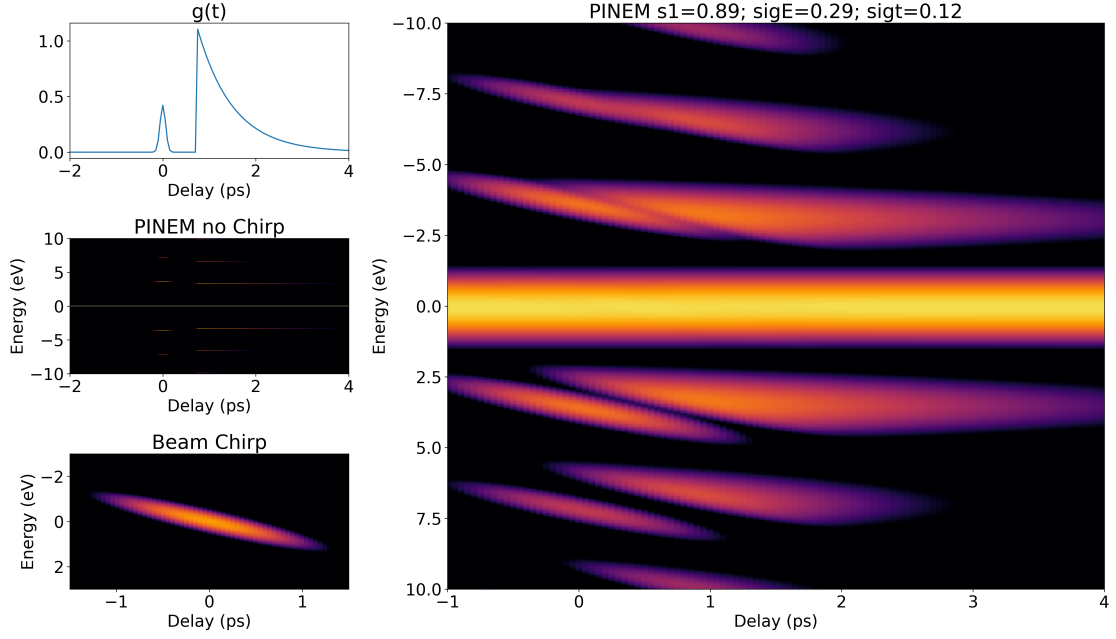


**Fig. 10** Different steps of the chirp simulation. a)  $g(t)$  distribution without chirp, which correspond to the deconvoluted signal of the  $P=0.66$  mW of Figure 3 of the main text. b) PINEM expected from the two models explain previously and with the value  $g(t)$  of a). c) Representation of the chirp from equation 4. d) Convolution of the beam chirp of c) and the PINEM of b).

## 5.5 Photoluminescence Spectrum during PINEM experiment

One PINEM map or delay scan is about 15 min, therefore the damage of a NWL under optical pumping as to be taken into account when doing multiple measurement of the same NWL. As explained in the main text the electron energy spectrum is recorded simultaneously with the photoluminescence, which allows us to track the evolution of the lasing emission properties for the duration of the scan. Figure 11 shows the luminescence spectrum of the four delay scans represented in Figure 2 and 3 of the main text.

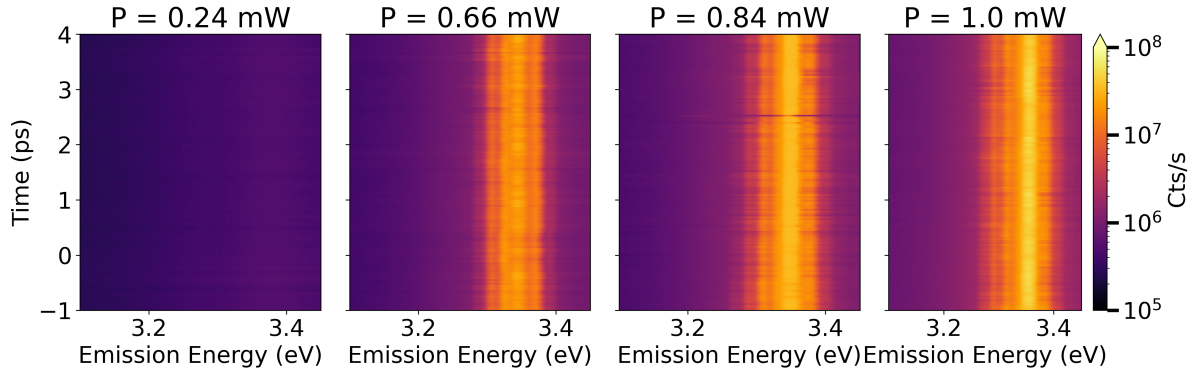


**Fig. 11** Photoluminescence spectrum recorded for every step of the delay scan used for Figure 2 and 3 of the main text. We can see that for the injection powers 0.66 mW, 0.84 mW and 1.0 mW the NWLs is lasing at 3.3 eV and the emitted mode are stable for the all duration of the measurement. While for the injection power of 0.24 mW the NWLs is below the lasing threshold for the all duration of the delay scan. The emission spectrum depicted Figure 1 and Figure 3 are the sum over all the time step of the experiment.

In the same fashion, for the PINEM maps recorded at a fixed delay between the pump laser and the electron beam, the PL spectrum was recorded for every pixels the average spectrum is shown in Figure 12.

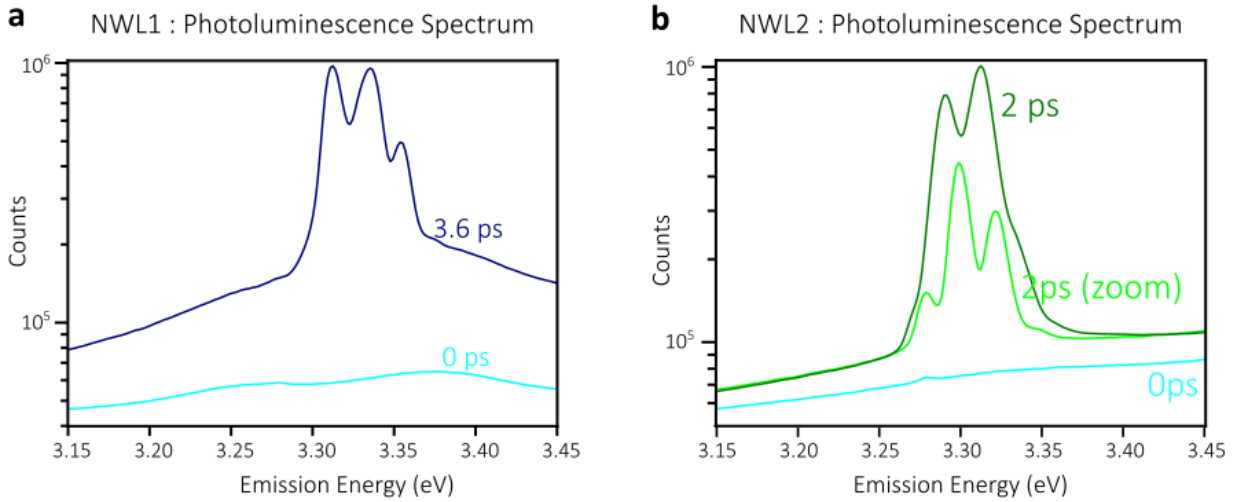


**Fig. 12 Average Photoluminescence Spectrum data of Figure 4.** a) Photoluminescence of NWL1 for the map recorded respectively at 0 ps ( $P = 0.34$  mW) and 3.6 ps ( $P = 0.31$  mW). b) Photoluminescence of NWL2 for the map recorded respectively at 0 ps ( $P = 0.94$  mW), 2.1 ps ( $P = 0.88$  mW) and for the zoom around the top at 2.1 ps ( $P = 1.2$  mW)

We note that the power used for the map at  $t = 0$  ps is higher than the power used for the first map at  $t = 2.1$  ps. We recorded the PINEM map at  $t = 0$  ps, once the NWL stopped lasing due to damage. Indeed the map at 0 ps doesn't depend on the lasing properties but only on the scattering of the pump laser on the structure (see Figure 2 of the main text). We can also see that despite both are FP modes, as shown on the map of Figure 4, the modes lasing for the two maps at 2.1 ps are not the same.

Figure 13 shows the intensity vs power within the same condition of illumination within the UTEM on another NWL in the same TEM grid. The characteristic S-shape expected for a lasing transition is recorded.

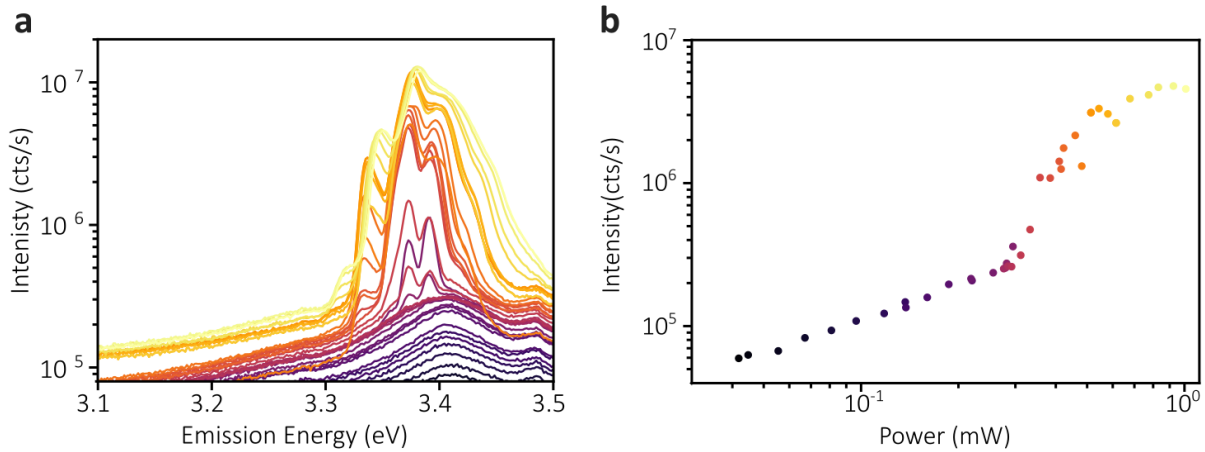


**Fig. 13** a) Photoluminescence Spectrum of a NWL depending on the laser power. b) Intensity between 3.3 eV and 3.49 eV depending on power.

## 5.6 Supplementary Data EELS study and data analysis

The EELS maps shown in Figure 4-a of the main text are fitted maps from an hyperspectral dataset of NWL4. Figure 14 shows the projection of the spectrum along the growth direction as well as the projection of a second set of data along the perpendicular direction showing the top of the nanowire. We clearly see the two behaviors explained in the main text.

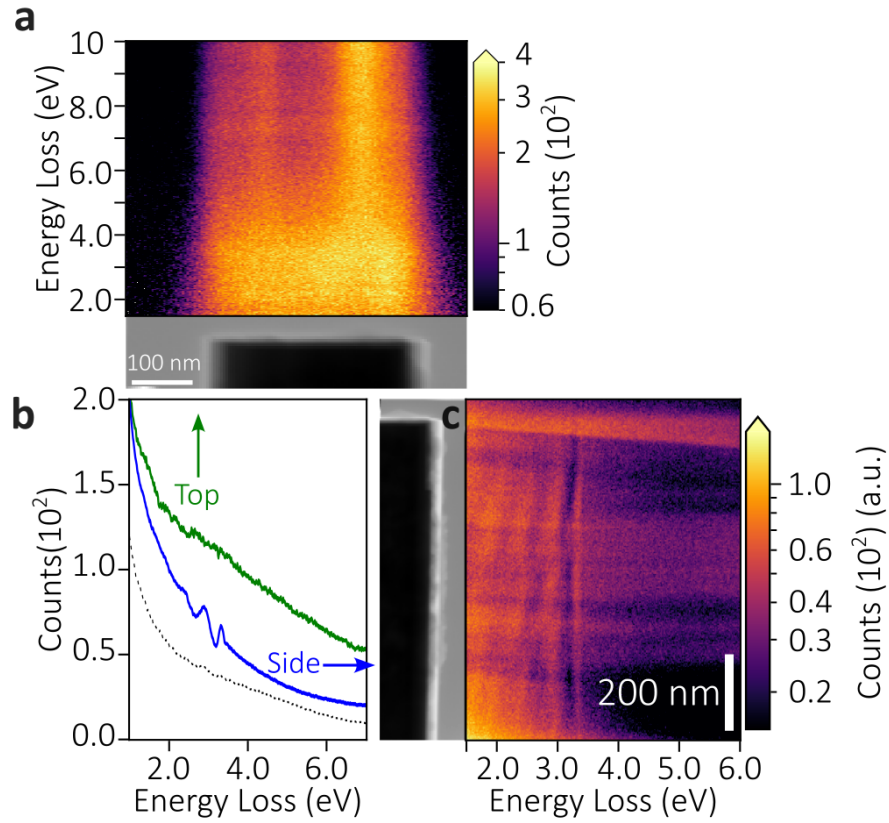


**Fig. 14** EELS Spectral projections of a- the top of the nanowire and b-along the growth direction. The WGM are clearly visible along the side of the NWL while the top show what it seems to be a continuum of FPM.

## 5.7 EELS Data from NWL 1

The EELS spectrum presented in Figure 3 of the main text is extracted from an hyperspectral dataset taken on NWL1. The Spectrum of Figure 3 is taken from the same position than the PINEM delay scan. The rest of the hyperspectral data are summarized on the Figure 15. We can see the whispering gallery mode visible on the EELS spectrum of Figure 3 visible along the NWL on the projection map of Figure 15-c.

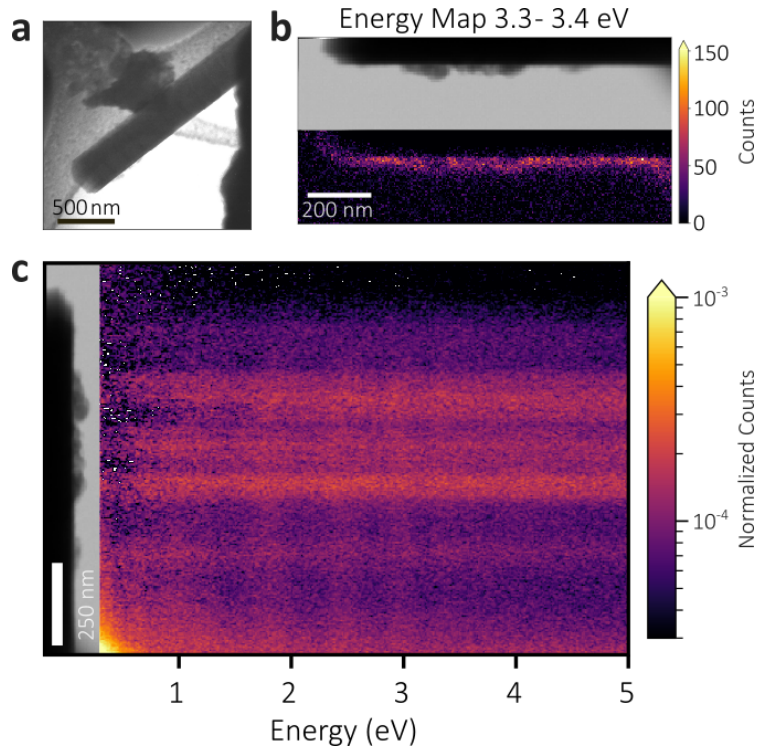


**Fig. 15 Monochromated EELS hyperspectral study of NWL1.** a) Bright Field (BF) Image Low Magnification b) Energy Map extracted from the data set from 3.3 to 3.4 eV with the corresponding BF image. c) Projection of the EELS Dataset along the NWL1 and after normalization and subtraction of the background.

## 5.8 Delay Scan without Electron chirp above the lasing threshold

We present here some data taken without chirp on another NWL. The laser power used for photoemission was significantly reduced in order to reduce the number of electrons produced at the tip to less than one electron per pulse.

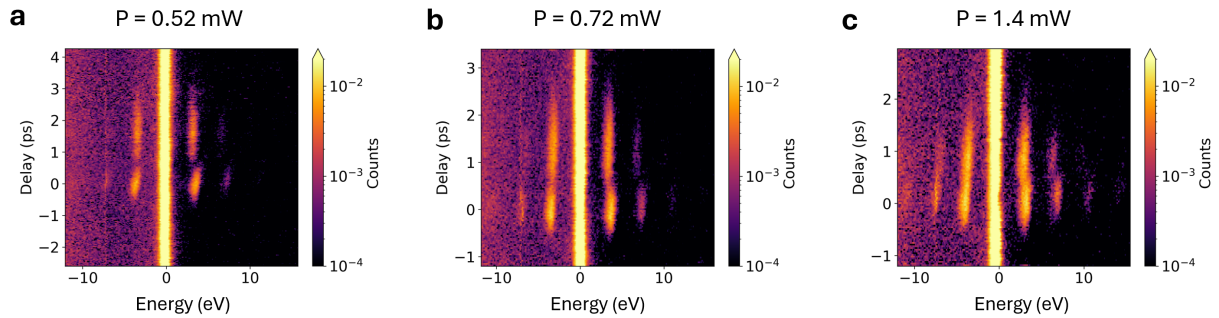


**Fig. 16 Delay scan of NWL5** Delay scan where the photoemission condition were set to reduce the chirp to minimum. Delay scan at the same position for different pump power :  $P = 0.52$  mW (a),  $P = 0.72$  mW (b),  $P = 1.4$  mW (c).

Figure 16 shows delay scans for a minimum chirp of the electron beam, we can see no tilt of the first side band corresponding to the scattering of the laser. The second set also does not show widening with delay, unlike the data presented in Figure 2 of the main article.